

See discussions, stats, and author profiles for this publication at: <https://www.researchgate.net/publication/262338011>

Theoretical Investigation of H-2 Oxidation on the Sr₂Fe_{1.5}Mn_{0.5}O₆ (001) Perovskite Surface under Anodic Solid Oxide Fuel Cell Conditions

ARTICLE in JOURNAL OF THE AMERICAN CHEMICAL SOCIETY · MAY 2014

Impact Factor: 12.11 · DOI: 10.1021/ja502629j · Source: PubMed

CITATIONS

8

READS

43

8 AUTHORS, INCLUDING:



[Salai Cheettu Ammal](#)
University of South Carolina
55 PUBLICATIONS 810 CITATIONS

[SEE PROFILE](#)



[Ana B Munoz-Garcia](#)
University of Naples Federico II
29 PUBLICATIONS 294 CITATIONS

[SEE PROFILE](#)



[Fanglin Chen](#)
University of South Carolina
184 PUBLICATIONS 3,068 CITATIONS

[SEE PROFILE](#)



[Andreas Heyden](#)
University of South Carolina
64 PUBLICATIONS 2,723 CITATIONS

[SEE PROFILE](#)

Theoretical Investigation of H₂ Oxidation on the Sr₂Fe_{1.5}Mo_{0.5}O₆ (001) Perovskite Surface under Anodic Solid Oxide Fuel Cell Conditions

Suwit Suthirakun,[†] Salai Cheettu Ammal,[†] Ana B. Muñoz-García,^{‡,⊥} Guoliang Xiao,[§] Fanglin Chen,[§] Hans-Conrad zur Loye,^{||} Emily A. Carter,[⊥] and Andreas Heyden^{†,*}

[†]Department of Chemical Engineering, University of South Carolina, 301 Main Street, Columbia, South Carolina 29208, United States

[‡]Department of Chemical Sciences, University of Naples Federico II, Naples 80126, Italy

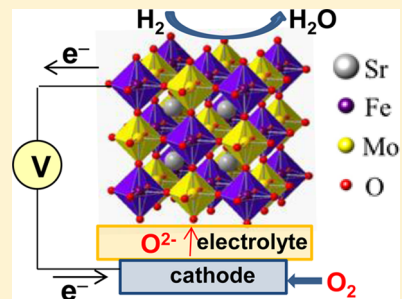
[§]Department of Mechanical Engineering, University of South Carolina, 300 Main Street, Columbia, South Carolina 29208, United States

^{||}Department of Chemistry and Biochemistry, University of South Carolina, 631 Sumter Street, Columbia, South Carolina 29208, United States

[⊥]Department of Mechanical and Aerospace Engineering, Program in Applied and Computational Mathematics, and Andlinger Center for Energy and the Environment, Princeton University, Princeton, New Jersey 08544, United States

S Supporting Information

ABSTRACT: Periodic density functional theory (DFT) calculations and microkinetic modeling are used to investigate the electrochemical oxidation of H₂ fuel on the (001) surface of Sr₂Fe_{1.5}Mo_{0.5}O₆ (SFMO) perovskite under anodic solid oxide fuel cell conditions. Three surface models with different Fe/Mo ratios in the topmost layer—identified by ab initio thermodynamic analysis—are used to investigate the H₂ oxidation mechanism. A microkinetic analysis that considers the effects of anode bias potential suggests that a higher Mo concentration in the surface increases the activity of the surface toward H₂ oxidation. At operating voltage and anodic SOFC conditions, the model predicts that water desorption is rate-controlling and that stabilizing the oxygen vacancy structure increases the overall rate for H₂ oxidation. Although we find that Mo plays a crucial role in improving catalytic activity of SFMO, under fuel cell operating conditions, the Mo content in the surface layer tends to be very low. On the basis of these results and in agreement with previous experimental observations, a strategy for improving the overall electrochemical performance of SFMO is increasing the Mo content or adding small amounts of an active transition metal, such as Ni, to the surface to lower the oxygen vacancy formation energy of the SFMO surface.



INTRODUCTION

Solid oxide fuel cells (SOFCs) are considered one of the most promising alternative energy technologies because they can efficiently convert chemical energy into electrical energy. Moreover, SOFCs can utilize a wide variety of fuels, such as H₂, natural gas, liquid fuels, biofuels, and gasified coal, with a relatively low sensitivity to fuel impurities compared with other types of fuel cells.^{1–4} The most commonly used material for SOFC anodes is Ni/YSZ (yttria-stabilized zirconia) cermet because Ni provides excellent catalytic activity and current collectability, and YSZ provides good ionic conductivity and structural support. Despite the advantages of the Ni/YSZ anode, this anode material encounters several limitations, such as instability upon redox cycling,⁵ nickel coarsening at high operating temperatures,^{6–8} sulfur poisoning,⁹ and carbon deposition when exposed to practical hydrocarbon fuels.¹⁰ Therefore, finding a suitable replacement for the conventional Ni/YSZ anode is currently a key objective in the development of SOFC technology.

Recently, Sr₂Fe_{1.5}Mo_{0.5}O_{6-δ} (SFMO) perovskite has been proposed as a promising anode material for SOFCs because this mixed ionic and electronic conductor (MIEC) pairs good catalytic activity with very good ionic and electrical conductivity.^{11–13} The mixed-valent Mo⁵⁺/Mo⁶⁺ and Fe³⁺/Fe⁴⁺ provide electronic conductivity, and the characteristic high oxygen vacancy concentration as well as low oxygen ion migration barriers in SFMO lead to a high ionic conductivity.^{12,13} The ionic conductivity of SFMO is significantly higher than that of the commonly used La_{0.8}Sr_{0.2}MnO₃ cathode, and its electrical conductivity in both air and hydrogen environments meets the conductivity requirements for both anodes and cathodes.^{14,15}

In a combined experimental and theoretical study, Muñoz-García et al.¹² identified a high concentration of constitutional oxygen vacancies in the SFMO bulk material as the likely source for boosting oxygen ion diffusion. Furthermore, their

Received: March 14, 2014

Published: May 14, 2014

theoretical analysis suggested that the formation of oxygen vacancies is promoted by the presence of relatively weak Fe–O bonds and a fully delocalized rearrangement of the extra charge delivered to the lattice upon removal of the neutral oxygen atom. Electronic structure analysis further revealed that the empty states across the Fermi energy in the SFMO conduction band are retained at experimental vacancy concentrations, leading to adequate electronic conductivity. The oxide ion diffusion kinetics characterized by first-principles calculations predicted an oxide ion migration barrier of only ~ 0.3 eV, much lower than the 0.8/0.9 eV of most other ABO_3 perovskites, including the parent material SrFeO_3 .¹³ Although these studies provide evidence for the MIEC character of the SFMO material, a detailed understanding of the electrocatalytic activity of this material is not yet available.

Experimental studies have shown that the SFMO anode can process both H_2 fuel and natural gas with high thermodynamic stability, and tolerance to sulfur.^{11,16} In addition, it was reported that SFMO displayed good thermal compatibility with the $\text{La}_{0.8}\text{Sr}_{0.2}\text{Ga}_{0.83}\text{Mg}_{0.17}\text{O}_3$ (LSGM) electrolyte.¹¹ However, its relatively low electro-oxidation activity is a major drawback which contributes to an overall low cell performance. Adding a small amount of Ni to the anode was found to be essential in achieving good performance, indicating that Ni has an electrocatalytic effect toward fuel oxidation on the SFMO surface.¹¹ The reasons behind the relatively poor electrochemical activity of SFMO and the role of Ni metal in improving the catalytic performance are currently unclear. Considering that understanding the fuel oxidation mechanism on perovskite surfaces such as SFMO is crucial for the development of alternative oxide based anode catalysts, it is the objective of this computational study to investigate the electrochemical fuel oxidation mechanism on the SFMO anode under realistic fuel cell operating conditions and to understand the role of Ni in improving its catalytic activity.

We aim at illustrating how a combination of a density functional theory (DFT)-based method and mean-field microkinetic modeling can be used to systematically study the H_2 oxidation mechanism on SFMO surfaces and determine the rate controlling step under SOFC operating conditions. We find that H_2O desorption, which produces surface oxygen vacancies, is rate-controlling under fuel cell operating conditions, and an SFMO surface with higher Mo concentration in the gas-exposed surface layer exhibits higher catalytic activity. Finally, Ni facilitates the surface oxygen vacancy formation process on the SFMO surface, which is found to be rate-controlling.

■ MODELS AND METHODS

Crystallographic Data of $\text{Sr}_2\text{Fe}_{1.5}\text{Mo}_{0.5}\text{O}_6$. The structure of $\text{Sr}_2\text{Fe}_{1.5}\text{Mo}_{0.5}\text{O}_6$ was initially reported as a cubic double perovskite structure in space group $Fm\text{-}3m$ with lattice parameter $a = 7.8717(1)$ Å.¹⁷ The crystal structure was studied using a Rietveld refinement of powder X-ray diffraction data. The typical formula of a double perovskite oxide is $A_2\text{BB}'\text{O}_6$, where the A-site cations are larger than the B- and B'-site cations and similar in size to the oxygen anions. The occupancies of the B and B' sites retained essentially the 3:1 ratio of Fe to Mo, as indicated by the empirical formula. More recently, Rietveld refinement of powder neutron diffraction data carried out by Bugaris et al. established that the room temperature structure of $\text{Sr}_2\text{Fe}_{1.5}\text{Mo}_{0.5}\text{O}_6$ belongs to space group $I4/mcm$ of the tetragonal system.¹⁸ The $I4/mcm$ space group contains only one B metal site, analogous to the case of a simple perovskite (ABO_3). The difference between the tetragonal and cubic structures arises from the MO_6 octahedra's having four

short and two long M–O bond distances coupled with octahedral tilting. Although these experiments clearly suggest that the room temperature $\text{Sr}_2\text{Fe}_{1.5}\text{Mo}_{0.5}\text{O}_6$ structure is tetragonal, computations based on DFT+U theory suggest that the cubic $Fm\text{-}3m$ and orthorhombic $Pnma$ structures (and therefore, also tetragonal structures) are essentially degenerate.¹² The differences in absolute energies and energies of oxygen vacancy formation between cubic and orthorhombic structures are negligible (<0.2 meV/f.u.). Moreover, in situ neutron diffraction experiments established that $\text{Sr}_2\text{Fe}_{1.5}\text{Mo}_{0.5}\text{O}_6$ undergoes a structural phase transition and takes on the cubic $Pm\text{-}3m$ ($Fm\text{-}3m$ in a double perovskite setting) structure by 400 °C.¹⁸ Therefore, in this work, all SFMO (001) surface models have been created from optimized lattice parameters of $Fm\text{-}3m$ cubic structure.

Computational Details. All calculations were carried out using spin-polarized DFT+U theory with periodic boundary conditions as implemented in the Vienna Ab initio Simulation Package (VASP 5.2).^{19,20} We chose the Perdew–Burke–Ernzerhof (PBE)²¹ functional to describe exchange and correlation effects. The nuclei and core electronic states were described by projector augmented-wave (PAW) potentials,²² and the Sr 4s4p5s, Fe 3p3d4s, Mo 4p5s4d, Ni 4s3d, and O 2s2p were treated as valence electrons. The plane wave basis set was found to be converged to within 1 meV per formula unit of SFMO at a kinetic energy cutoff of 800 eV. Integration over the first Brillouin zone used Gaussian smearing ($\sigma = 0.05$ eV) during structural relaxations. The U–J parameter was employed to correct the self-interaction error inherent in pure DFT when applied to transition metals with tightly localized d electrons, such as Fe in SFMO. In accordance with earlier computational studies on SFMO,^{12,23} we set the U–J value for Fe to 4.0 eV and used no U–J parameter for Mo, as validated on the parent SrFeMoO_6 compound.

The bulk structure of SFMO was optimized using a pseudocubic cell of 40 atoms ($\text{Sr}_8\text{Fe}_6\text{Mo}_2\text{O}_{24}$) with a $4 \times 4 \times 4$ Monkhorst–Pack (MP)²⁴ k-mesh. This model has the required minimum size to study the 3:1 Fe/Mo ratio. Figure 1(a,b) illustrates the two possibilities for

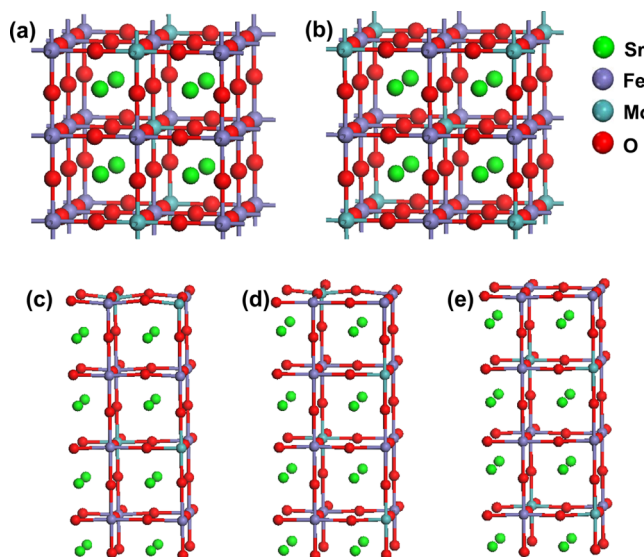


Figure 1. (Top) $\text{Sr}_2\text{Fe}_{1.5}\text{Mo}_{0.5}\text{O}_6$ cubic supercells of bulk SFMO with different distributions of Mo atoms: (a) plane-Mo configuration and (b) diagonal-Mo configuration. (Bottom) SFMO (001) surface models constructed from the two bulk models: (c) plane-Mo surface, (d) diagonal-Mo surface, and (e) FeO_2 -terminated surface.

Fe and Mo distributions in this bulk SFMO model. The two configurations represent planar (Figure 1a) and diagonal (Figure 1b) distributions of Mo atoms in the bulk, and thus, we name these configurations plane-Mo and diagonal-Mo, respectively. The calculated PAW–PBE+U lattice constants, $a = 7.880$ Å and $a = 7.922$ Å for the plane-Mo and diagonal-Mo bulk configurations, respectively, are in close agreement with experimental and previous theoretical values.¹²

We find that the antiferromagnetic arrangement of Fe spins is the most stable arrangement in both configurations. The optimized lattice parameters were then used to construct stoichiometric (1×1) surface slab models with eight atomic layer thickness (Figure 1(c–e)). Only the $(\text{Fe}/\text{Mo})\text{O}_2$ termination is considered in the surface slab models because they are expected to be more catalytically active than the SrO -terminated surface.

In addition to the plane-Mo (Figure 1c) and diagonal-Mo (Figure 1d) surface models, the plane-Mo bulk configuration provides another possibility to construct a surface slab model with FeO_2 termination (Figure 1e). For clarity, we refer to this slab model as FeO_2 -terminated surface. The number of Mo atoms in the top surface layer of the plane-Mo, diagonal-Mo, and FeO_2 -terminated surfaces are 2, 1, and 0, respectively. Each slab model contains two SFMO bulk unit cells ($\text{Sr}_{16}\text{Fe}_{12}\text{Mo}_4\text{O}_{48}$) in the surface normal direction. A vacuum gap of 15 Å was used to minimize the interaction between images along the z -axis. The bottom-most layer was fixed in all calculations to mimic a semi-infinite bulk crystal. Test calculations suggested that fixing the bottom layer gives rise to only small dipole corrections (<0.1 eV). The surface slabs were optimized using a $4 \times 4 \times 1$ MP k-mesh. By increasing the number of k-points to $5 \times 5 \times 1$, we observed a negligibly small change in oxygen vacancy formation energy (<0.01 eV), suggesting a very good convergence of reaction energies with respect to the k-mesh density. Dipole and quadrupole corrections to the energy are taken into account using a modified version of the Markov and Payne method,²⁵ that is, the contribution of dipole interactions along the z -axis is subtracted from the total energy. Transition state (TS) structures of various elementary steps were optimized using the climbing image nudge-elastic band (CI-NEB)²⁶ and dimer methods.^{27–29}

Finally, we note that test calculations on a symmetric slab display a negligible difference of <0.07 eV in oxygen vacancy formation energy compared with that of using the asymmetric slab with a dipole correction scheme (see Supporting Information). This indicates that the dipole correction scheme used in our calculations works properly and reaction energies can be predicted accurately with an asymmetric slab model.

Microkinetic Model. Transition state theory was used to calculate the forward and backward rate constants for a surface reaction $A^* \rightarrow B^*$,

$$k_{\text{for}} = A_{\text{for}} e^{-E_{\text{for}}^{\text{a}}/k_{\text{B}}T}; \quad k_{\text{rev}} = A_{\text{rev}} e^{-E_{\text{rev}}^{\text{a}}/k_{\text{B}}T} \quad (1)$$

where $E_{\text{for}}^{\text{a}}$ and $E_{\text{rev}}^{\text{a}}$ denote the zero-point energy (ZPE)-corrected forward and reverse activation barriers, respectively. The ZPE was obtained as $\sum(1/2)\hbar\nu_i$ from calculated vibrational frequencies, ν_i . All adsorbed species and the nearest neighbor atoms of the SFMO surface model that are directly involved in the reaction mechanism were included in the frequency calculations (see Figure S2 in the Supporting Information). Displacements of ± 0.001 Å were used along the x , y , and z directions for all Hessian constructions from analytic gradients. From the calculated frequencies, we confirmed the nature of a first-order saddle point with one imaginary frequency. Frequency factors (A) were calculated from the vibrational partition functions (q_{vib}) using the following expressions:

$$A_{\text{for}} = \frac{k_{\text{B}}T}{h} \frac{q_{\text{vib},\text{TS}}}{q_{\text{vib},\text{A}^*}}; \quad A_{\text{rev}} = \frac{k_{\text{B}}T}{h} \frac{q_{\text{vib},\text{TS}}}{q_{\text{vib},\text{B}^*}};$$

$$(q_{\text{vib}}) = \prod_i \frac{1}{1 - e^{-hv_i/k_{\text{B}}T}} \quad (2)$$

For an adsorption process, $\text{A} + * \rightarrow \text{A}^*$, where $*$ represents an empty site on the surface model and A^* is the adsorbed species, collision theory was used to calculate the adsorption (forward) rate constant, $k_{\text{for}} = (10^5/(2\pi m_A k_{\text{B}} T)^{1/2}) S_{\text{unit}} (\text{s}^{-1} \text{atm}^{-1})$, where m_A is the molecular weight of species A and k_{B} is the Boltzmann's constant. We assumed a sticking coefficient of 1 in all simulations. S_{unit} is the surface area of our slab model, which is equal to $6.20 \times 10^{-19} \text{ m}^2$. The reverse rate constant was obtained from the relation $K = k_{\text{for}}/k_{\text{rev}}$, where K is the equilibrium constant calculated from the ZPE-corrected adsorption

energy (ΔE_{ads}) and the entropy factors of gas molecule (A) using the expression, $K = (q_{\text{vib},\text{A}^*}/q_{\text{vib}})(q_{\text{vib},\text{rot},\text{trans}})_A e^{-\Delta E_{\text{ads}}/k_{\text{B}}T}$.

Once the forward and reverse rate constants of each elementary step were computed, a master equation was constructed and solved for the steady-state solution of probability densities for the system to occupy each discrete state. In the following, we call these probability densities surface coverages, θ . The BzzMath library developed by Buzzi-Ferraris³⁰ was used to solve the steady-state equations. The calculated surface coverages were further used to compute the rates of all elementary steps at specific reaction conditions. The apparent activation energy (E_{app}) was calculated over a temperature range of 900–1300 K using the expression,

$$E_{\text{app}} = RT^2 \left(\frac{d \ln r_{\text{overall}}}{dT} \right)_{P,y_i} \quad (3)$$

where the total pressure (P) and the mole fraction of species i in the reaction mixtures (y_i) are kept constant. The “degree of rate control” for step i , $X_{\text{RC},i}$ was calculated using Campbell's theory^{31,32} as

$$X_{\text{RC},i} = \frac{k_i}{r} \left(\frac{r}{k_i} \right)_{K_i, k_{j \neq i}} \quad (4)$$

where the equilibrium constant for step i (K_i) and all other rates ($k_{j \neq i}$) are held constant. Similarly, the “degree of thermodynamic rate control” of an intermediate, n , was calculated as

$$X_{\text{TRC},n} = \frac{1}{r} \left(\frac{r}{\left(\frac{-G_n^0}{RT} \right)} \right)_{G_m^0 \neq n, G_i^0 \text{ TS}} \quad (5)$$

where the Gibbs free energy of all other intermediates ($m \neq n$) and all transition states (i) are held constant.

RESULTS AND DISCUSSION

Ab Initio Thermodynamic Analysis. The three surface models shown in Figure 1(c–e) are used to investigate the electro-oxidation of H_2 under SOFC operating conditions. The different surface Mo concentrations of these three surfaces will allow us to understand the effect of Mo on the electrocatalytic activity of SFMO. In agreement with earlier computational studies of bulk SFMO,^{12,13} the three surface models constructed here also exhibit metallic character. The calculated energies of these stoichiometric surfaces (Table 1) suggest that

Table 1. Relative Energies of Stoichiometric^a and Reduced Surfaces^b of the Three Surface Models of SFMO Calculated with DFT+U

surface models of SFMO	relative energy (eV)	
	stoichiometric surface $\text{Sr}_{16}\text{Fe}_{12}\text{Mo}_4\text{O}_{48}$	reduced surface $\text{Sr}_{16}\text{Fe}_{12}\text{Mo}_4\text{O}_{43}$
plane-Mo	0.00	0.00
diagonal-Mo	1.08	-0.89
FeO_2 -terminated	1.26	-1.72

^a $\text{Sr}_2\text{Fe}_{1.5}\text{Mo}_{0.5}\text{O}_6$, Figure 1. ^b $\text{Sr}_2\text{Fe}_{1.5}\text{Mo}_{0.5}\text{O}_{6-\delta}$, $\delta = 0.675$, Figure 2.

the stability of these surfaces decreases in the order plane-Mo surface > diagonal-Mo surface > FeO_2 -terminated surface. However, earlier studies identified a high concentration of constitutional oxygen vacancies and a low oxygen migration barrier in this material, which were proposed to be largely responsible for high oxygen ion diffusivity.^{12,13} In addition, SOFCs are operated at high temperatures (>1000 K) and reducing conditions (low oxygen partial pressures). Under

these reducing conditions, multiple oxygen vacancies are expected to be present in the SFMO material. In fact, in situ powder neutron diffraction experiments on the SFMO material revealed that oxygen loss occurs on heating the sample in a wet hydrogen atmosphere, and the stoichiometry of the material at 850 °C was identified as $\text{Sr}_2\text{Fe}_{1.5}\text{Mo}_{0.5}\text{O}_{5.5}$ while heating in 4% H_2 .¹⁸ To understand the nature of the three selected SFMO surface models under SOFC operating conditions, we carried out a constrained ab initio thermodynamic analysis by creating multiple oxygen vacancies at various locations and constructed approximate phase diagrams. Different possible spin arrangements of Fe atoms in the surface models were tested whenever an additional oxygen vacancy was created to identify the most stable magnetic configuration.

Constrained ab initio atomistic thermodynamics calculations, which compute Gibbs free energies, allow us to identify relevant structures and compositions under realistic temperatures and pressures that constitute starting points for a later detailed investigation of reaction pathways. The phase diagrams were constructed by calculating the free energies of reaction 6 as a function of oxygen chemical potential, that is, temperature and oxygen partial pressure.



where δ denotes the number of oxygen vacancies in the surface model ($\delta = 1-6$). The Gibbs free energy for the formation of an oxygen vacancy can be computed as

$$\Delta G = E_{\text{red}} + \delta[E_{\text{O}} + \Delta\mu_{\text{O}}(T, P)] - E_{\text{full}} \quad (7)$$

where E_{red} is the DFT+U electronic energy of the structure with oxygen vacancies ($\text{Sr}_{16}\text{Fe}_{12}\text{Mo}_4\text{O}_{48-\delta}$) and E_{full} is the DFT+U electronic energy of the stoichiometric slab. We define the energy of atomic oxygen, E_{O} , to be half of the energy of an oxygen molecule, E_{O_2} , which is obtained from the H_2O splitting reaction using the experimental reaction energy and DFT energies of H_2 and H_2O in the gas phase,^{33,34}

$$E_{\text{O}_2} = 2[(E_{\text{H}_2\text{O}}^{\text{DFT}} + E_{\text{H}_2\text{O}}^{\text{ZPE}}) - (E_{\text{H}_2}^{\text{DFT}} + E_{\text{H}_2}^{\text{ZPE}}) - E_{\text{hof}}] - E_{\text{O}_2}^{\text{ZPE}} \quad (8)$$

Here, E^{ZPE} is the experimental zero-point energy,³⁵ E_{hof} is the experimental heat of formation of a gas-phase H_2O molecule ($T = 0$ K),³⁵ and E^{DFT} is the energy calculated with PBE functional. This semiempirical estimate of the energy of atomic oxygen allows us to avoid the well-known errors associated with using DFT-PBE to directly calculate either E_{O_2} or E_{O} (self-interaction, spin contamination, etc.). The chemical potential of O, which includes the temperature- and pressure-dependent free energy contributions of the O_2 molecule, is described by $\Delta\mu_{\text{O}}(T, P)$ and has been calculated from first-principles using the rotational, translational, and vibrational partition functions of the O_2 molecule. We neglect all zero-point energies in eq 7 (other than those explicitly appearing in eq 8) and assume that entropic contributions from the solids to the free energy difference are insignificant.³⁶⁻³⁸ In addition, the pressure dependence of $\Delta\mu_{\text{O}}(T, P)$ is obtained assuming that the gas phase is ideal.

$$\Delta\mu_{\text{O}}(T, P) = \frac{1}{2}\left(\Delta\mu_{\text{O}}(T, P^0) + k_{\text{b}}T \ln\left(\frac{P}{P^0}\right)\right) \quad (9)$$

Figure 2 illustrates the calculated phase diagrams for the plane-Mo (Figure 2a), diagonal-Mo (Figure 2b), and FeO_2 -

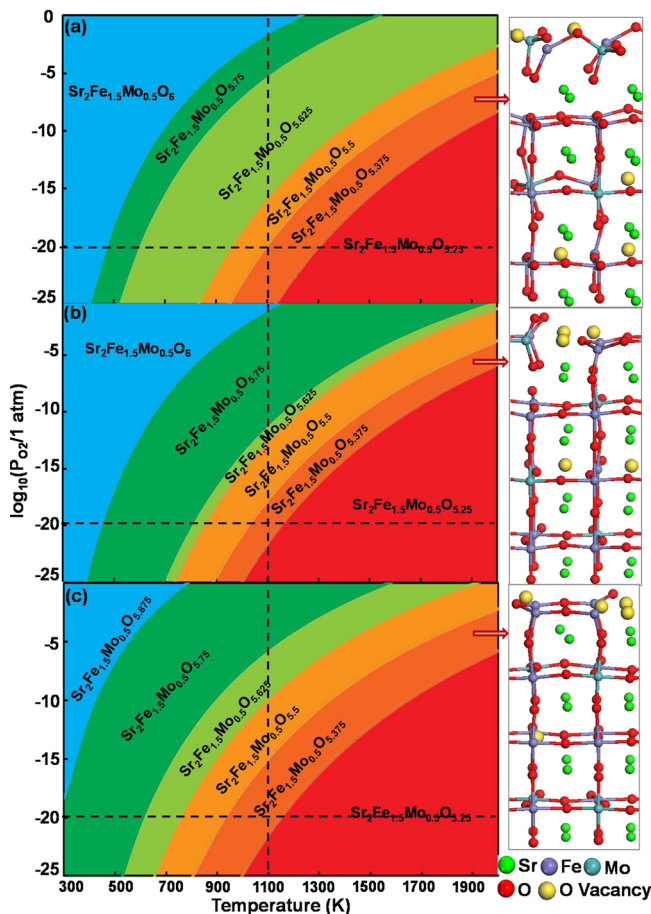


Figure 2. Calculated phase diagrams of SFMO surfaces: (a) plane-Mo surface, (b) diagonal-Mo surface, and (c) FeO_2 -terminated surface. Differently shaded areas mark the stability regions of various structures for a given temperature and partial pressure of oxygen. Dashed lines indicate experimental anodic SOFC conditions ($T = 1100$ K and $P_{\text{O}_2} = 10^{-20}$ atm).³⁹ The optimized structures on the right correspond to the most stable $\text{Sr}_2\text{Fe}_{1.5}\text{Mo}_{0.5}\text{O}_{6-\delta}$ ($\delta = 0.625$) structure of each surface model.

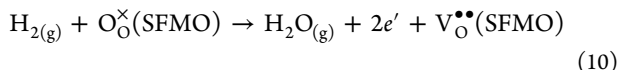
terminated (Figure 2c) surface models. At relevant SOFC operating conditions ($P_{\text{O}_2} = 10^{-20}$ atm, $T = 1100$ K),³⁹ all three surface models possess five oxygen vacancies. The optimized structures of the three slab models with five oxygen vacancies are shown next to the corresponding phase diagrams in Figure 2. We note here that we tried all meaningful oxygen vacancy positions in the process of identifying the lowest-energy structures. In the lowest-energy structures with five oxygen vacancies, the distribution of vacancy sites is different in the three surface models. The plane-Mo surface (Figure 2a) has two oxygen vacancies in the topmost layer, whereas the diagonal-Mo (Figure 2b) surface has three oxygen vacancies, and the FeO_2 -terminated (Figure 2c) surface contains four oxygen vacancies on the topmost layers. We note that structures with surface oxygen vacancies are generally more stable than structures with bulk oxygen vacancies because of the ability of the surface to restructure. Two types of oxygen vacancies ($\text{V}_\text{O}^{••}$, in Kröger-Vink notation⁴⁰)—those between a Mo and a Fe atom ($\text{Mo}-\text{V}_\text{O}^{••}-\text{Fe}$) and those between two Fe

atoms ($\text{Fe}-\text{V}_\text{O}^{\bullet\bullet}-\text{Fe}$)—can be formed in SFMO. Our calculations suggest that the oxygen vacancy formation energies of $\text{Mo}-\text{V}_\text{O}^{\bullet\bullet}-\text{Fe}$ are higher than those of $\text{Fe}-\text{V}_\text{O}^{\bullet\bullet}-\text{Fe}$. These results are in agreement with previously reported calculations that mid-to-late transition metals, such as Fe, form much weaker metal–oxygen bonds than early transition metals, such as Mo.¹² As a result, Fe–O bonds are easier to break to remove oxygen from the lattice and generate a vacancy. Thus, the plane-Mo surface with high Mo concentration in the surface that possesses only Mo–O–Fe bonds in the surface prefers to form only two oxygen vacancies. The other two surfaces with higher Fe concentration in the surface prefer to form three and four oxygen vacancies in the surface layer.

Furthermore, we find that the three reduced surface configurations with five oxygen vacancies exhibit different thermodynamic stabilities compared with their corresponding stoichiometric surfaces. Table 1 lists the relative DFT+U energies of stoichiometric surfaces and reduced surfaces with five oxygen vacancies. It can be seen that the plane-Mo surface configuration is preferred under synthesized conditions (relatively high oxygen chemical potentials), whereas diagonal-Mo and Fe-terminated surface configurations predominate under SOFC operating environments (relatively low oxygen chemical potentials). This indicates that under anodic SOFC conditions, the relative concentration of Mo atoms in the surface layer should be lower than in the bulk SFMO material. Although our thermodynamic analysis suggests that the FeO_2 -terminated surface is the most stable surface under SOFC operating conditions, we performed a mechanistic study of all three reduced surfaces to understand the effect of Mo content on H_2 electro-oxidation.

H₂ Oxidation Mechanism on SFMO (001) Surfaces.

The three SFMO surface configurations considered in this study offer different types of active sites on each surface for H₂ oxidation. For example, the active oxygen involved in the H₂ oxidation mechanism on a plane-Mo surface is bonded to Mo and Fe (Mo—O—Fe) and on the FeO₂-terminated surface the active oxygen is bonded to two Fe atoms (Fe—O—Fe). However, the diagonal-Mo surface possesses both types of oxygen atoms, and thus, we considered two different active sites (Mo—O—Fe and Fe—O—Fe) for this surface model. The overall electrochemical oxidation of H₂ at the SFMO anode can be expressed (in Kröger-Vink notation⁴⁰) as



where $V_O^{\bullet\bullet}$ denotes a doubly charged oxygen vacancy on the surface and the two electrons of O_O^{\times} (oxygen on the surface) are transferred via the M–O–Fe ($M = Fe$ or Mo) bridge to the current collector. Figure 3 illustrates our proposed catalytic cycle for the oxidation of H_2 on the SFMO (001) surface model and the reaction steps involved in the surface reaction at an active site, $*_M-O-Fe$ ($M = Mo$ or Fe), are described in eqs R1–R3. We note here that all DFT+U calculations have been performed on charge-neutral surface models, and we considered electrochemical charge transfer only in our microkinetic model. Thus, the net charge on both sides of all reactions (R1–RS) described below is zero.

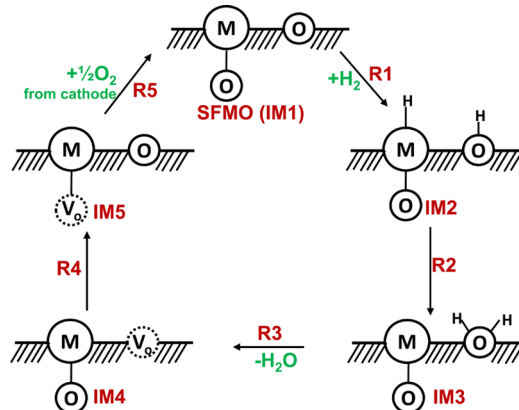
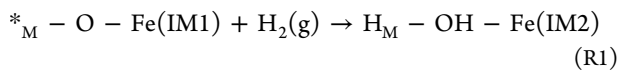
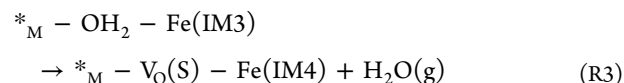
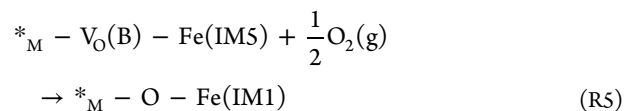
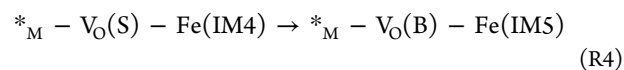


Figure 3. Proposed mechanism for H₂ oxidation on Sr₂Fe_{1.5}Mo_{0.5}O₆ surface.



In the first step (R1), a H₂ molecule from the feed gas adsorbs dissociatively on a metal site (Mo or Fe) and a neighboring oxygen atom, forming a hydroxyl species on the surface. In this context, our calculations suggest that molecular adsorption of H₂ and dissociative adsorption of H₂ on one metal site are energetically unfavorable. The H atom on the metal site is then transferred to the hydroxyl species (R2), forming a H₂O molecule. H₂O desorption from the surface (R3) creates a surface oxygen vacancy (V_O(S); we did not use Kröger–Vink notation⁴⁰ in the reaction mechanism at the anode because it is not clear at this point when charge transfer occurs). Although the H₂ oxidation process is completed in these three steps, the kinetics of this reaction cannot be examined unless the catalytic cycle is completed. Thus, in our model, we also included the process of oxygen ion migration from SFMO bulk to the surface oxygen vacancy (R4) and the bulk oxygen vacancy (V_o(B)) being filled by an oxygen ion from the cathode (R5).



The replenishment of bulk oxygen vacancy (R5) involves at least two elementary steps. The first step involves the reduction of oxygen at the cathode–electrolyte interface, which transfers the oxygen ion to the electrolyte ($(1/2 \text{ O}_{2(\text{g})} + \text{V}_{\text{el}}^{\bullet\bullet} + 2e^- \rightarrow \text{O}_{\text{el}}^\times)$, followed by the exchange of an oxygen ion from electrolyte to the anode, filling the bulk oxygen vacancy ($\text{O}_{\text{el}}^\times + \text{V}_{\text{SFMO}}^{\bullet\bullet} \rightarrow \text{O}_{\text{SFMO}}^\times + \text{V}_{\text{el}}^{\bullet\bullet}$). In our model, we assume that the current collection and oxygen reduction reaction at the cathode (first step) are fast under SOFC operating conditions, which is justified by the experimental observation that addition of Ni to the anode surface significantly improves the overall cell performance, that is, the anode is performance-limiting. Because the ionic conductivity of SFMO is comparable to the commonly used electrolyte $\text{La}_{0.8}\text{Sr}_{0.2}\text{Ga}_{0.83}\text{Mg}_{0.17}\text{O}_3$ (LSGM) in the perovskite-based fuel cells,^{41–43} we considered the bulk oxygen diffusion barrier of SFMO as the limiting factor in the

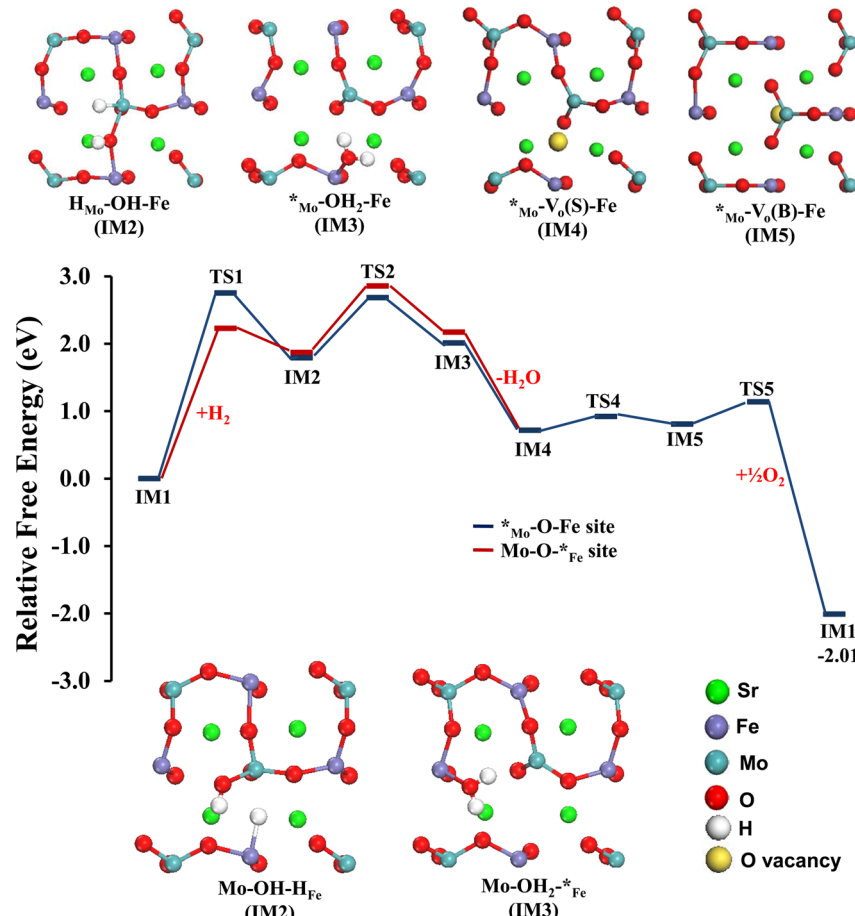


Figure 4. Free energy profile (eV) for the H_2 oxidation reaction on the plane-Mo surface of SFMO ($T = 1100 \text{ K}$; $P_i(\text{gas}) = 1 \text{ atm}$). All energies are with reference to the sum of the energies of the initial state (IM1) and the gas phase molecules. The insets provide a top view of the optimized structures of the intermediates.

oxygen ion exchange process and used this barrier to calculate the rate of reaction (R5). The bulk oxygen diffusion barrier of SFMO is calculated on the basis of the structures reported in our previous work¹³ as 0.33 eV.

Reaction Pathways and Energetics of H_2 Oxidation on SFMO (001) Surfaces. The plane-Mo slab model (Figure 2a) has six Mo–O–Fe type oxygen atoms on the surface. We chose one of those oxygen atoms that has the lowest oxygen vacancy formation energy as the active site for H_2 oxidation. We tested and confirmed that the spin configurations on all Fe atoms do not change along the reaction coordinate, and we used the optimized spin configuration of our reactant surface models (IM1) for each surface termination to describe the magnetic behavior of all intermediates. The Gibbs free energy profile calculated at $T = 1100 \text{ K}$ for H_2 oxidation on the plane-Mo surface is provided in Figure 4. The partial pressures of the gas phase molecules were assumed to be 1 atm. The intermediate structures are shown in the inset, and the transition state structures are provided in the Supporting Information. The TS structures are numbered with reference to the elementary reaction steps throughout this paper.

Dissociative adsorption of H_2 (R1) was initially considered on Mo and the neighboring oxygen atom, which leads to the formation of IM2 ($\text{H}_{\text{Mo}}\text{—OH—Fe}$). At 1100 K, this process is endergonic by 1.79 eV (R1, $\Delta E_{\text{ZPE}} = 0.20 \text{ eV}$) and has an activation free energy as high as 2.75 eV. The transfer of an H atom from Mo to the hydroxyl group (R2) is also an

endergonic process ($\Delta G = 0.22 \text{ eV}$) and has a barrier of 0.89 eV. The H_2O molecule formed in this process prefers to be bonded to the Fe atom rather than Mo, as illustrated in the structure IM3. Desorption of this H_2O molecule from the plane-Mo surface takes place in the following step (R3), creating a surface oxygen vacancy (IM4). This step is exergonic by -1.29 eV ($\Delta E_{\text{ZPE}} = 0.99 \text{ eV}$).

Next, we considered the migration of a bulk oxygen ion from the subsurface layer to the surface oxygen vacancy in the following step (R4), which creates a bulk oxygen vacancy (IM5). The bulk oxygen vacancy structure is only 0.11 eV higher in free energy compared with the surface oxygen vacancy structure, and this migration process has an activation barrier of 0.20 eV. The catalytic cycle is completed by filling this bulk oxygen vacancy by an oxygen ion from the cathode in step R5. As explained in the previous section, we added a barrier of 0.33 eV to this process that corresponds to the SFMO bulk oxygen diffusion barrier.¹³ The free energy difference between the two IM1 states (-2.01 eV) in Figure 4 is the free energy of the hydrogen oxidation reaction, $\text{H}_{2(\text{g})} + 1/2 \text{ O}_{2(\text{g})} \rightarrow \text{H}_2\text{O}_{(\text{g})}$, calculated at 1100 K and $P_i(\text{gas}) = 1 \text{ atm}$.

In addition to this pathway, we have also tested the possibility of dissociating an H_2 molecule on a Fe–O species instead of a Mo–O species in reaction step R1. The corresponding structures and free energies for this possibility are provided in Figure 4. Although the intermediate formed in this process, $\text{Mo}\text{—OH—H}_{\text{Fe}}$, is slightly less stable than

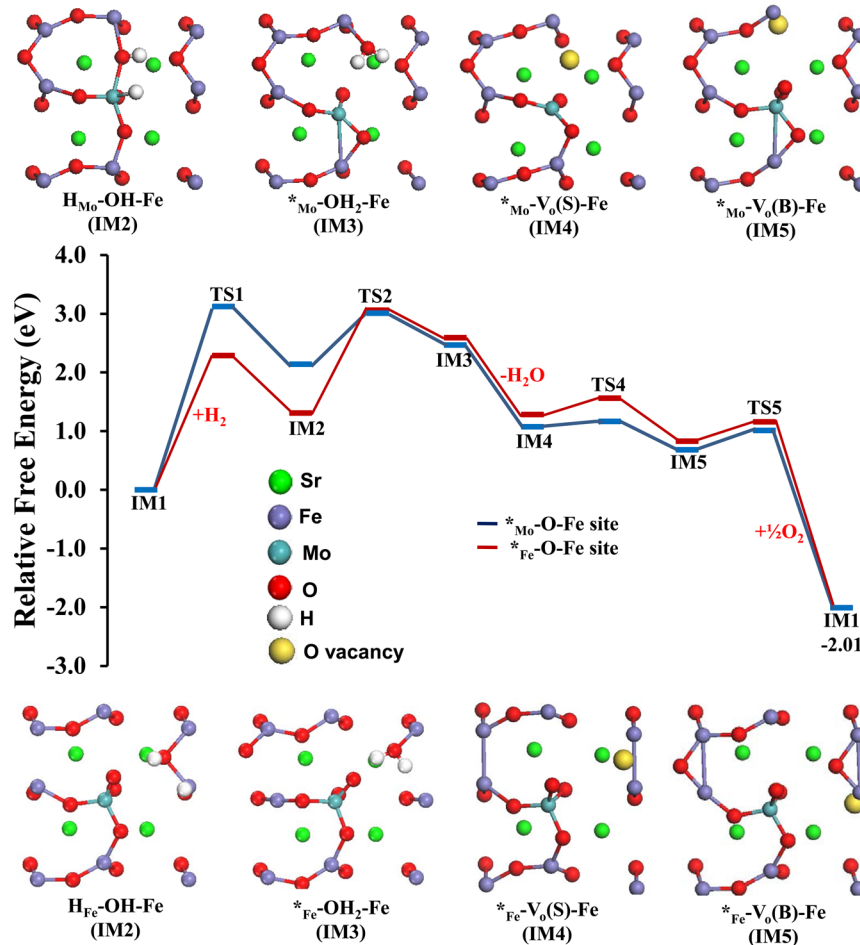


Figure 5. Free energy profile (eV) for the H_2 oxidation on the diagonal-Mo surface of SFMO ($T = 1100 \text{ K}$; $P_{\text{i(gas)}} = 1 \text{ atm}$). All energies are with reference to the sum of the energies of the initial state (IM1) and the gas phase molecules. The insets provide a top view of the optimized structures of the intermediates.

intermediate $\text{H}_{\text{Mo}}-\text{OH}-\text{Fe}$ by 0.08 eV, the activation barrier for dissociating H_2 at the Fe–O site is lower than that of a Mo–O site. However, transferring the H atom from Fe to the –OH group has a higher activation barrier compared with the H_2O formation process at the Mo–O site (R2). Overall, the highest energy state in the free energy profile of the Mo–O pathway corresponds to the H_2 dissociation process (TS1), whereas it is the H_2O formation TS (TS2) for the Fe–O pathway. Because TS2 of the Fe–O pathway is 0.11 eV higher in energy compared with TS1 of the Mo–O pathway, the Mo–O pathway is expected to be preferred over the Fe–O pathway. Furthermore, our microkinetic analysis suggested that the overall rates calculated for the Fe–O pathway are slightly lower than for the Mo–O pathway, and thus, we did not include the Fe–O pathway in the following analysis.

The diagonal-Mo slab model (Figure 2b) possesses three Mo–O–Fe type oxygen atoms and two Fe–O–Fe type oxygen atoms. We chose one Mo–O–Fe active site and one Fe–O–Fe active site for investigating the H_2 oxidation mechanism (the ones with the smallest oxygen vacancy formation energies). The calculated Gibbs free energy profiles for these two active sites together with the intermediate structures are provided in Figure 5. Compared with the plane-Mo surface, the TS structures corresponding to both the H_2 dissociation process (R1) and the H_2O formation process (R2) at the Mo–O–Fe site of the diagonal-Mo surface are ~0.4–0.5 eV higher in free

energy. The reaction energy profiles further suggest that the surface oxygen vacancy structure ($\text{Mo}-\text{V}_o(\text{S})-\text{Fe}$) on the diagonal-Mo surface is about 0.35 eV less stable than that of the plane-Mo surface. A comparison of reaction energetics between the Mo–O–Fe and Fe–O–Fe sites on the diagonal-Mo surface reveals that the H_2 dissociation process (R1) is favored on the Fe–O–Fe site, whereas the H_2O formation process (R2) is favored on the Mo–O–Fe site. Overall, the higher activation barriers and less stable intermediates suggest that the H_2 oxidation process is less favorable on the diagonal-Mo surface compared with the plane-Mo surface.

On the FeO_2 -terminated surface (Figure 2c), only four oxygen atoms of Fe–O–Fe type exist, and thus, we chose the one with smallest oxygen vacancy formation energy for our mechanistic investigation. The Gibbs free energy profile illustrated in Figure 6 reveals that the reaction energetics for this pathway is similar to the one for the Fe–O–Fe site on the diagonal-Mo surface. Here again, the TS corresponding to H_2O formation (TS2) has the highest energy in the free energy profile, and its relative stability is even lower than the corresponding TS on the diagonal-Mo surface.

Insights from Microkinetic Modeling. The thermochemical data and activation barriers obtained from DFT+U calculations suggest that the H_2 oxidation process could be more favorable on a plane-Mo surface compared with the diagonal-Mo and FeO_2 -terminated surfaces; however, we

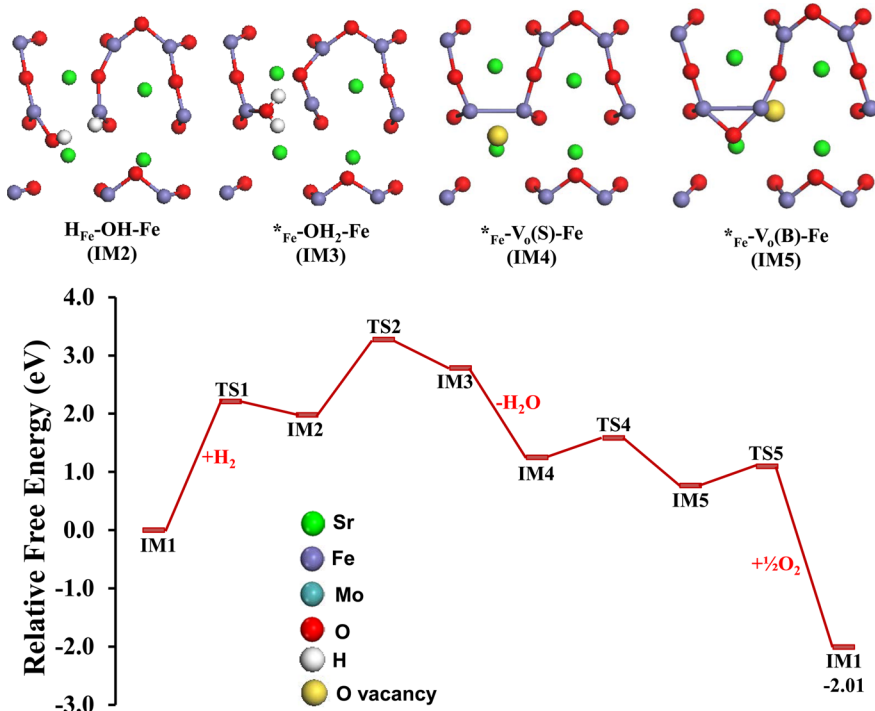


Figure 6. Free energy profile (eV) for the H_2 oxidation reaction on the FeO_2 -terminated surface of SFMO ($T = 1100 \text{ K}$; $P_{\text{i(gas)}} = 1 \text{ atm}$). All energies are with reference to the sum of the energies of the initial state (IM1) and the gas phase molecules. The insets provide a top view of the optimized structures of the intermediates.

Table 2. Forward Rate Constants (k_{for}) and Equilibrium Constants (K) Calculated at 1100 K for the Elementary Steps of H_2 Oxidation on SFMO Surfaces

reaction step	plane-Mo surface		diagonal-Mo surface		FeO_2 -terminated surface	
	${}^*\text{Mo}-\text{O}-\text{Fe}$ site		${}^*\text{Mo}-\text{O}-\text{Fe}$ site		${}^*\text{Fe}-\text{O}-\text{Fe}$ site	
	$k_{\text{for}} (\text{s}^{-1})$	K	$k_{\text{for}} (\text{s}^{-1})$	K	$k_{\text{for}} (\text{s}^{-1})$	K
R1	1.21×10^1	6.28×10^{-9}	6.59×10^0	9.59×10^{-9}	8.61×10^3	5.21×10^{-5}
R2	9.67×10^9	3.20×10^0	3.82×10^9	7.34×10^{-2}	8.06×10^4	1.52×10^{-6}
R3	9.86×10^{11}	8.56×10^2	6.32×10^{12}	5.48×10^3	2.31×10^{12}	2.01×10^3
R4	1.71×10^{12}	5.51×10^{-1}	1.64×10^{12}	9.06×10^0	2.00×10^{11}	5.41×10^2
R5	6.76×10^{11}	1.68×10^{14}	6.76×10^{11}	4.62×10^{13}	6.76×10^{11}	1.87×10^{13}

cannot deduce the most active surface from DFT+U energies alone because the relative rates on these surfaces depend on the reaction conditions, such as temperature and partial pressure of reactant molecules. More importantly, for the electro-oxidation reactions in SOFCs, we also need to consider the presence of electric fields and the effect of anode potential bias on the reaction mechanism. The reaction free energies of the elementary steps that involve charge transfer processes are directly affected by the potential bias. It is currently unknown how the charge is transferred from the SFMO surface to the external circuit and which elementary steps are involved one or two electron charge transfer. To first understand the effect of experimentally relevant conditions on the H_2 oxidation reaction on different surfaces and also to obtain detailed information on the relative rates, activation barriers, and rate-controlling steps, we initially built a DFT+U based microkinetic model, including the five elementary steps (R1–R5) without considering the effect of anode bias potential. The reaction free energies, activation barriers, entropies of surface intermediates, and frequency factors are the parameters required for describing the model. Table 2 summarizes the calculated forward rate and equilibrium constants of these elementary steps on the three

SFMO surfaces. The calculated rate constants are used to solve the steady-state master equation, which gives the fractional surface coverages of all adsorbed species and the fraction of free sites.

The temperature range used in this study is between 900 and 1300 K, and the partial pressure of reactant molecules at the anode are typical experimental conditions of $P_{\text{H}_2} = 1 \text{ atm}$ and $P_{\text{H}_2\text{O}} = 0.03 \text{ atm}$, whereas the oxygen partial pressure at the cathode is assumed to be 0.21 atm. The calculated rates and other insights obtained from the microkinetic analysis at a representative temperature of 1100 K are summarized in Table 3. In the absence of anode bias potential, the model predicts that the ${}^*\text{Mo}-\text{O}-\text{Fe}$ active site on the plane-Mo surface exhibits a higher reaction rate and lower apparent activation barrier than the diagonal-Mo and FeO_2 -terminated surfaces under SOFC operating conditions. Campbell's degree of rate control analysis indicates that H_2 dissociation (R1) is the rate-controlling process when the reaction occurs via Mo–O active sites, whereas H_2O formation (R2) is rate-controlling when the reaction occurs via Fe–O active sites for all three surfaces. Furthermore, Campbell's degree of thermodynamic rate control

Table 3. Calculated Rates, Apparent Activation Barriers (E_{app}), Degree of Rate Control (X_{RC}), and Degree of Thermodynamic Rate Control (X_{TRC}) for H₂ Oxidation on SFMO Surfaces Obtained from Microkinetic Analysis at 1100 K^a

surface model	active site	overall rate (s ⁻¹)	E_{app} (eV)	X_{RC}		X_{TRC}
				R1	R2	* _M —O—Fe (IM1)
plane-Mo	* _{Mo} —O—Fe	10.1	1.11	0.8	0.2	-1.0
diagonal-Mo	* _{Mo} —O—Fe	5.58	1.54	0.8	0.2	-1.0
	* _{Fe} —O—Fe	4.10	1.48	0.0	1.0	-1.0
FeO ₂ -terminated	* _{Fe} —O—Fe	5.91	1.73	0.0	1.0	-1.0

^a $P_{H_2} = 1$ atm and $P_{H_2O} = 0.03$ atm.

analysis reveals that the overall rate is sensitive mostly to the stability of the reactant structure (SFMO).

Effects of Anode Bias Potential. For modeling the electrochemical oxidation of H₂ on SFMO surfaces, as discussed above, we also need to consider the presence of an electrochemical double layer that is induced by the potential drop across the anode/electrolyte interface. The electric field interacts with the surface intermediates and, thus, can change the adsorption energy of different species. In this regard, Linic and co-workers^{44,45} have shown that the electric field effect on the binding energies of O and OH on Ni is <0.15 eV and that there is no effect on the adsorption energy of H in the presence of typical electric field strengths expected in SOFCs (<0.5 V/Å). This is not surprising because these adsorbates are not expected to be very ionic, so as primarily neutral species, they should be unaffected by electric fields. We expect a similar trend in the H adsorption energy on SFMO surfaces and, thus, neglected this effect in our calculations. In addition to the electric field effect on adsorption energies, the free energy of surface intermediates is influenced by the anode potential bias, affecting the free energies of elementary steps that involve charge transfer. The chemical potential of species after charge transfer is shifted by the amount of charge multiplied by the electrical potential. For example, for the electrochemical oxidation of H₂ on the SFMO surface (H_{2(g)} + O_O^X (SFMO) → H_{2O(g)} + 2e⁺ + V_O^{••} (SFMO), eq 10), the Gibbs free energy is calculated as

$$\Delta G = G(H_2O) + G(V_O^{••}) + 2e\Delta V - G(H_2) - G(O_O^X) \quad (11)$$

where $G(H_2O)$ and $G(H_2)$ are the free energies of H_{2O} and H₂ gas molecules, and $G(V_O^{••})$ and $G(O_O^X)$ are the free energies of the SFMO surfaces with and without a surface oxygen vacancy, respectively. ΔV is the cell voltage, which is the difference between the cathode potential and the anode potential ($\Delta V = V_{cathode} - V_{anode}$), and e is the magnitude of charge of an electron (1.60×10^{-19} C). At SOFC operating conditions of 800 °C, 0.21 atm cathode O₂ partial pressure, and 1 atm anode H₂ partial pressure, the free energy of reaction H₂ + 1/2 O₂ → H_{2O} is calculated as -2.2 eV.^{35,46} Because the electrochemical reactions at electrodes involve a transfer of two electrons per mole of H₂, the maximum open-circuit voltage (OCV) at these conditions is 2.2/2 = 1.1 V. This serves as a reference for electrode potential, and we fix the cathode equilibrium potential to be 1.1 V. Because the cathode potential is fixed,

eq 11 suggests that an increase in anode potential decreases the free energy of the elementary step involved in charge transfer. Furthermore, the activation barrier of the charge transfer step is also influenced by the anode bias potential, and the activation free energy of a charge transfer step, ΔG^\ddagger , is calculated as

$$\Delta G^\ddagger = \Delta G^{0,\ddagger} + n_i\beta\Delta V \quad (12)$$

where $\Delta G^{0,\ddagger}$ is the activation free energy of the elementary step at short circuit conditions (without the effect of bias potential); n_i represents the number of transferred electrons in the charge transfer step; and β is the symmetry factor, which ranges from 0 to 1 and describes approximately the influence of the electrode potential on the free energy of the transition state of an elementary step.⁴⁷ We have considered $\beta = 0$ and $\beta = 0.5$ in the present study and found that both possibilities provide similar results at operating voltage $\Delta V > 0.7$ V. The results presented here are calculated with $\beta = 0$, that is, we assumed that the charge transfer is a fast process that can occur at any point in time, which we consider most suitable for gas phase electrochemistry. The results obtained with $\beta = 0.5$, which is an average choice in the absence of more information, are provided in the Supporting Information. We note that a symmetry factor of zero does not mean that the overall charge transfer coefficient (α) is zero. The forward (k_f) and reverse (k_r) rate constants of the charge transfer step are then calculated as

$$k_f = A_f \exp\left(\frac{-\Delta G_f^{0,\ddagger} - n_i\beta\Delta V}{RT}\right);$$

$$k_r = A_r \exp\left(\frac{-\Delta G_r^{0,\ddagger} - n_i(1-\beta)\Delta V}{RT}\right) \quad (13)$$

where A_f and A_r denote the frequency factors of the forward and reverse rates, respectively.

In our model, the surface electro-oxidation process described in eq 10 involves three elementary steps (R1–R3), and it is currently unclear which of these elementary steps involve the charge transfer process. Thus, we considered the possibility of one- or two-electron charge transfer on all of these three elementary steps, which adds an additional nine elementary steps. The calculated rate constants for these additional steps are then included in our microkinetic model to recalculate the surface coverages and rates. We chose a representative temperature of 1100 K and varied the cell voltage, ΔV , from 0.1 to 1.1 V for this analysis. All elementary steps included in our microkinetic model with different charge transfer possibilities and the calculated rates at a representative cell voltage of 0.7 V are provided in the Supporting Information. Our microkinetic analysis reveals that both one- and two-electron charge transfer during the H₂ oxidation process (R1) are not favorable. The rates calculated for the elementary steps suggest that a two-electron charge transfer during H_{2O} desorption R3 and two one-electron charge transfers during H_{2O} formation (R2) and H_{2O} desorption (R3) are competitive on the three surfaces when the cell voltage (ΔV) is varied from 0.1 to 1.1 V.

Table 4 summarizes the overall rates calculated for the three surfaces at a bias potential of $\Delta V = 0.7$ V and the rate control factors calculated using Campbell's analysis. A comparison of the values presented in Tables 3 and 4 indicates that the overall rates calculated at $\Delta V = 0.7$ V are ~4 orders of magnitude lower than the rates at short circuit condition ($\Delta V = 0$ V). The

Table 4. Overall Rates, Degree of Rate Control (X_{RC}), and Degree of Thermodynamic Rate Control (X_{TRC}) for H_2 Oxidation on SFMO Surfaces Calculated in the Presence of Anode Bias Potential^a

surface model	active site	overall rate (s^{-1})	X_{RC}	X_{TRC}
			R3	${}^*_{M-O-Fe}$ (IM1)
plane-Mo	${}^*_{Mo-O-Fe}$	2.26×10^{-2}	1.0	-1.0
diagonal-Mo	${}^*_{Mo-O-Fe}$	4.90×10^{-3}	1.0	-1.0
	${}^*_{Fe-O-Fe}$	2.08×10^{-4}	1.0	-1.0
FeO ₂ -termination	${}^*_{Fe-O-Fe}$	2.52×10^{-4}	1.0	-1.0

^a $T = 1100$ K; $P_{H_2} = 1$ atm; $P_{H_2O} = 0.03$ atm; $\Delta V = 0.7$ V.

plane-Mo surface still exhibits the highest overall rate for H_2 electro-oxidation compared with the other two surfaces. Although the thermodynamic rate control analysis points to the same initial reactant surface structure as the most important intermediate, the rate control analysis in the presence of a bias potential ($\Delta V = 0.7$ V) indicates that the H_2O desorption process, which corresponds to surface oxygen vacancy formation, is the rate-controlling process on all surfaces.

Next, we examined the effect of cell voltage on the rates and rate-controlling factors by simulating the polarization curves that reflect the kinetic relationship between cell voltage and current density. The current density is calculated using the relation, $i = zer\Gamma$, where i denotes the current density ($A\text{ cm}^{-2}$), z is the number of electron(s) involved in the reaction, r represents the calculated overall reaction rate (s^{-1}), and Γ is the number of active sites per surface area (cm^{-2}). We assume that there is no ohmic loss or mass diffusion limitation because the cell is operated at very high temperatures and SFMO is an excellent electron and ion conductor. Figure 7 illustrates the

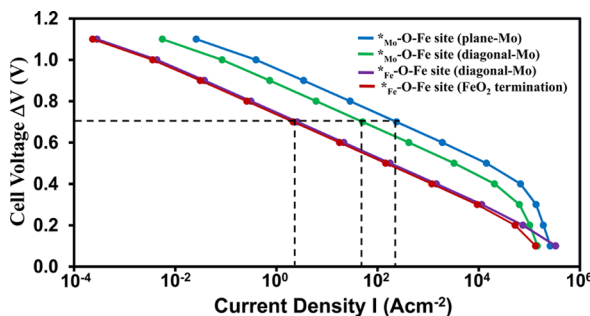


Figure 7. Calculated polarization curves (current per surface area of the individual surface models) for H_2 oxidation on SFMO (001) surfaces ($T = 1100$ K). Dashed line indicates the current density at an operating voltage of 0.7 V.

simulated polarization curves for the three surfaces. The current density decreases with increasing cell voltage, and at operating voltage ($\Delta V = 0.7$ V), the current density calculated for the plane-Mo surface ($2.37 \times 10^2 \text{ A cm}^{-2}$) is higher than the current density for the other two surfaces. Except at low voltage conditions ($\Delta V < 0.2$ V), the calculated current densities are very similar for the ${}^*_{Fe-O-Fe}$ site on the diagonal-Mo and FeO₂-terminated surfaces.

Campbell's degree of rate control analysis (Figure 8) indicates that the rate-controlling process on the three surfaces changes with the operating voltage. At cell voltages close to short-circuit conditions, H_2 dissociation or H_2O formation are identified as the rate-controlling steps; however, at SOFC operating voltages ($\Delta V \geq 0.7$ V), H_2O desorption (i.e., the surface oxygen vacancy formation process) becomes rate-controlling on all surface models. Thus, the activity of these surfaces can be related to the ability to form surface oxygen vacancies under SOFC operating conditions, as illustrated in Table 5. In other words, the calculated current densities

Table 5. Gibbs Free Energies (ΔG) for the Formation of an Oxygen Vacancy in the SFMO (001) Surface under Reducing Conditions^a and the Calculated Current Density at $\Delta V = 0.7$ V

surface model	Mo content (%)	active site	ΔG (eV)	current density ($A\text{ cm}^{-2}$)
plane-Mo	50	${}^*_{Mo-O-Fe}$	0.52	236.95
diagonal-Mo	25	${}^*_{Mo-O-Fe}$	0.92	50.72
		${}^*_{Fe-O-Fe}$	1.10	2.15
FeO ₂ -termination	0	${}^*_{Fe-O-Fe}$	1.07	2.61

^a $*_{M-O-Fe} + H_2 \rightarrow {}^*_{M-V_O(S)-Fe}$ (IM4) + H_2O , $T = 1100$ K, $P_{gas} = 1$ atm.

correlate well with the Gibbs free energies of the reaction, $*_{M-O-Fe}$ (IM1) + $H_2(g) \rightarrow {}^*_{M-V_O(S)-Fe}$ (IM4) + $H_2O(g)$ on the three surfaces. Interestingly, surface oxygen vacancy formation is facilitated on the surface with higher Mo concentration, indicating that Mo stabilizes the oxygen vacancy. This can be explained by Mo^{5+}/Mo^{6+} species (assuming formal charges) in the topmost surface layer being more easily reduced than Fe^{2+}/Fe^{3+} species. As a result, the plane-Mo surface with a higher Mo concentration in the surface layer is more active for H_2 electro-oxidation than the diagonal-Mo and FeO₂-terminated surfaces. However, our thermodynamic analysis (Table 1) suggested that the least active FeO₂-terminated surface is the stable surface under SOFC operating conditions, which explains the experimentally observed poor catalytic activity of this SFMO material. However, experimental studies

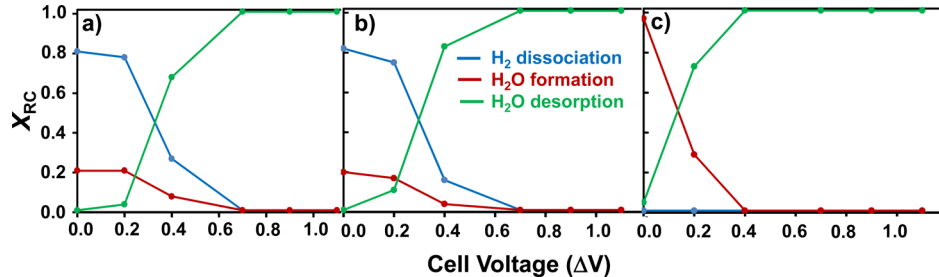


Figure 8. Campbell's degree of rate control (X_{RC}) analysis of H_2 oxidation on SFMO surfaces as a function of cell voltage ($T = 1100$ K): (a) ${}^*_{Mo-O-Fe}$ active site on plane-Mo surface, (b) ${}^*_{Mo-O-Fe}$ active site on diagonal-Mo surface, and (c) ${}^*_{Fe-O-Fe}$ active site on FeO₂-terminated surface.

Table 6. Calculated Bader Charges (e) on the Neighboring Metal and Oxygen Atoms of the Active Site on the Stoichiometric SFMO Surface ($\text{Sr}_{16}\text{Fe}_{12}\text{Mo}_4\text{O}_{48}$) and the Reduced Catalyst Models before ($\text{Sr}_{16}\text{Fe}_{12}\text{Mo}_4\text{O}_{43}$) and after ($\text{Sr}_{16}\text{Fe}_{12}\text{Mo}_4\text{O}_{42}$) Vacancy Formation^a

surface model	Bader charges (in e)		
	$\text{Sr}_{16}\text{Fe}_{12}\text{Mo}_4\text{O}_{48}$ (M–O–Fe)	$\text{Sr}_{16}\text{Fe}_{12}\text{Mo}_4\text{O}_{43}$ (M–O–Fe)	$\text{Sr}_{16}\text{Fe}_{12}\text{Mo}_4\text{O}_{42}$ (M–V * –Fe)
plane-Mo (Mo–O–Fe)	Mo	+2.52	+2.54
	Fe	+1.78	+1.32
	O ^{av}	-1.09	-1.06
FeO ₂ -termination (Fe–O–Fe)	Fe ^{av}	+1.76	+1.22
	O ^{av}	-1.12	-1.30
Ni ₂ /FeO ₂ -termination (Fe–O–Fe)	Fe ^{av}		+1.13
	O ^{av}		-1.27
	Ni ^{total}		+0.70
			+0.04

^aO^{av} entries indicate the average charge on the three nearest neighboring oxygen atoms, Fe^{av} entries indicate the average charge on the two neighboring Fe atoms of the active oxygen, and Ni^{total} entries indicate the total charge on the two Ni atoms.

have observed that the performance of this material can be dramatically improved by dispersing a small amount of Ni (~2 wt %) into the SFMO anode.¹¹ On the basis of our current analysis, we expect that addition of an active transition metal, such as Ni, to the SFMO surface could facilitate surface oxygen vacancy formation, which in turn improves the electrochemical performance toward H₂ oxidation. The ability of active transition metals to promote oxygen vacancy formation on metal oxide surfaces has been demonstrated by some of us for Au/TiO₂, Pt/TiO₂, Pt/CeO₂, and Ni/YSZ.^{33,48–51}

To better understand the effect of Ni on the surface oxygen vacancy formation process, we calculated the Gibbs free energies for the reaction ${}^*\text{Fe}-\text{O}-\text{Fe}$ (IM1) + H₂(g) → ${}^*\text{Fe}-\text{V}_\text{O}(\text{S})-\text{Fe}$ (IM4) + H₂O(g) on the FeO₂-terminated surface in the presence of one and two Ni adatoms. The optimized structures and the details of these calculations are provided in the Supporting Information. Our calculations suggest that the Ni atoms bind strongly to the surface oxygen atoms and promote the oxygen vacancy formation, even when the Ni atoms are not in direct contact with the active oxygen atom. In the presence of a Ni₂ dimer, the Gibbs free energy of the oxygen vacancy formation process, Fe–O–Fe + H₂(g) → Fe–V_o(S)–Fe + H₂O(g), was calculated to be 0.09 eV, which is nearly 1 eV lower than the free energy of reaction in the absence of Ni (Table S). Thus, these calculations confirm our hypothesis that Ni facilitates the surface oxygen vacancy formation process.

In the previous computational studies on the SFMO bulk material, Muñoz-García et al.^{12,13} explained the easier reduction of Fe–O–Fe bonds compared with Mo–O–Fe bonds in terms of delocalization of the extra charge in the lattice and the availability of strongly hybridized Fe 3d/O 2p states at the Fermi level. According to their analysis, Mo retains part of the extra charge and Fe tends to delocalize the charge by releasing it to the oxygen sublattice. However, in the already reduced surface models considered in the present study, Mo–O–Fe bonds are easier to reduce than the Fe–O–Fe bonds. To better understand the promotional effect of Mo on the plane-Mo surface and also the electronic effect of Ni on the FeO₂-terminated surface, we analyzed the electron density of these surfaces by computing Bader charges,^{52,53} which yields a qualitative picture of the reorganization of the electron density upon removal of a neutral oxygen atom. To identify the oxidation states of the Fe and Mo atoms in our catalyst surface models ($\text{Sr}_{16}\text{Fe}_{12}\text{Mo}_4\text{O}_{43}$), we compared their Bader charges (Table 6) with those in the stoichiometric surface models

($\text{Sr}_{16}\text{Fe}_{12}\text{Mo}_4\text{O}_{48}$). According to our thermodynamic analysis, the plane-Mo surface has only two oxygen vacancies on the surface and the remaining three oxygen vacancies are in the bulk (Figure 2a). Comparing the Bader charges in the first two columns of Table 6 for the plane-Mo surface, we can conclude that the creation of two oxygen vacancies in the surface reduced only the Fe atoms while the Mo atoms retained their high oxidation state Mo⁶⁺ (formal charges). Thus, it is possible to transfer the extra charge to these Mo atoms upon removal of an additional surface oxygen atom ($\text{Sr}_{16}\text{Fe}_{12}\text{Mo}_4\text{O}_{42}$) from Mo–O–Fe (last column of Table 6). We note that there is no significant change in the charge of the oxygen and Fe atoms during this process. In contrast, the FeO₂-terminated surface has four oxygen vacancies on the surface under SOFC operating conditions (Figure 2c), and a comparison of Bader charges on the stoichiometric ($\text{Sr}_{16}\text{Fe}_{12}\text{Mo}_4\text{O}_{48}$) and reduced surfaces ($\text{Sr}_{16}\text{Fe}_{12}\text{Mo}_4\text{O}_{43}$) suggests that all surface Fe atoms in the reduced surface are reduced from Fe³⁺ to Fe²⁺ (formal charges). Analogous to previous bulk SFMO results, there is also significant delocalization of the extra electrons to neighboring oxygen atoms in the first and second layers, making this surface model energetically more favorable than the plane-Mo surface model. Further removal of an oxygen atom ($\text{Sr}_{16}\text{Fe}_{12}\text{Mo}_4\text{O}_{42}$) from Fe–O–Fe during the catalytic cycle, however, reduces Fe from its stable Fe²⁺ state to an unstable Fe¹⁺ state (formal charge), making this process highly endergonic. When Ni is added to this surface ($\text{Sr}_{16}\text{Fe}_{12}\text{Mo}_4\text{O}_{43}$), Ni donates some electrons to the surface (mostly to the Fe atoms), as previously found by Shishkin and Ziegler for Ni adsorption on ceria.⁵⁴ Upon removing the additional oxygen atom, most of the extra charge is transferred back to Ni, and the Fe atoms are not significantly further reduced. Thus, both Ni and Mo promote oxygen vacancy formation by accepting the extra electrons left by the removed oxygen atom.

CONCLUSIONS

We developed a microkinetic model based on DFT+U-derived parameters that was able to explain the experimentally observed reaction behavior of SFMO anode electrodes and provided significant insights into the rate-controlling process during H₂ electro-oxidation. We employed constrained ab initio thermodynamic calculations to construct various surface models under SOFC operating conditions. Three surface models with varying Mo concentration in the surface layer were identified, which were then used to investigate the thermochemistry and reaction

barriers of the elementary steps involved in the H₂ electro-oxidation mechanism. To include the effect of anode bias potential, we included additional elementary steps in our microkinetic model, considering the possibility of one- or two-electron charge transfer processes at various elementary steps. Simulated polarization curves reflect the kinetic activity of SFMO surfaces and suggest that the plane-Mo surface is more active toward H₂ oxidation than the diagonal-Mo and FeO₂-terminated surfaces. Further analysis revealed that at relevant operating voltages and reaction conditions, water desorption is rate-controlling, and stabilizing the oxygen vacancy structure increases the overall rate.

In addition, an increase in activity is observed with increasing Mo content in the surface layer. The surface configuration with higher Mo concentration on the exposed layer has a lower oxygen vacancy formation energy because it is easier to reduce Mo⁶⁺ species than the already reduced Fe²⁺ species upon creating an oxygen vacancy on the surface. However, according to our thermodynamic analysis, the surface Mo concentration tends to be very low under anodic SOFC conditions, which explains the experimentally observed poor activity of SFMO. The presence of small Ni particles on the least active FeO₂-terminated surface dramatically reduces the surface oxygen vacancy formation energy by receiving the extra charge left by the oxygen atom. Consequently, increasing the Mo content or adding an active transition metal such as Ni to the SFMO surface should facilitate surface oxygen vacancy formation and lead to an improvement in overall electrochemical performance of the SOFC cell.

■ ASSOCIATED CONTENT

Supporting Information

Discussion on the use of an asymmetric versus symmetric slab model for the mechanistic study (Figure S1); intermediate structures highlighting the atoms displaced for vibrational frequency calculations (Figure S2), transition state structures involved in the H₂ oxidation reaction on the plane-Mo surface (Figure S3), diagonal-Mo surface (Figure S4) and FeO₂-terminated surface (Figure S5); reaction rates calculated for elementary steps with charge transfer possibility and a symmetry factor of $\beta = 0$ (Table S1); results computed with $\beta = 0.5$ (Table S2, Figure S6); effect of Ni on the oxygen vacancy formation energy (Figure S7); and the XYZ coordinates of selected structures. This material is available free of charge via the Internet at <http://pubs.acs.org>.

■ AUTHOR INFORMATION

Corresponding Author

E-mail: heyden@cec.sc.edu.

Notes

The authors declare no competing financial interest.

■ ACKNOWLEDGMENTS

This work was supported by the Heterogeneous Functional Materials Center (HeteroFoAM), an Energy Frontier Research Center (EFRC) funded by the U.S. Department of Energy, Office of Basic Energy Science under Award No. DE-SC0001061. Computations were carried out at the US Department of Energy facilities located at the National Energy Research Scientific Computing Center (NERSC) and at EMSL, located at Pacific Northwest National Laboratory (Grant Proposal 47447). Furthermore, a portion of this research was

performed with XSEDE resources provided by the National Institute for Computational Sciences (NICS) and Texas Advanced Computing Center (TACC) under Grant No. TG-CTS090100. Finally, computing resources from University of South Carolina NanoCenter and its High Performance Computing Group are gratefully acknowledged.

■ REFERENCES

- (1) Atkinson, A.; Barnett, S.; Gorte, R. J.; Irvine, J. T. S.; McEvoy, A. J.; Mogensen, M.; Singhal, S. C.; Vohs, J. *Nat. Mater.* **2004**, *3*, 17–27.
- (2) Minh, N. Q. *Solid State Ionics* **2004**, *174*, 271–277.
- (3) Minh, N. Q. *J. Am. Ceram. Soc.* **1993**, *76*, 563–588.
- (4) Singh, P.; Minh, N. Q. *Int. J. Appl. Ceram. Technol.* **2004**, *1*, 5–15.
- (5) Sarantaridis, D.; Atkinson, A. *Fuel Cells* **2007**, *7*, 246–258.
- (6) Iwata, T. *J. Electrochem. Soc.* **1996**, *143*, 1521–1525.
- (7) Tsoga, A.; Naoumidis, A.; Nikolopoulos, P. *Acta Mater.* **1996**, *44*, 3679–3692.
- (8) Simwonis, D.; Tietz, F.; Stover, D. *Solid State Ionics* **2000**, *132*, 241–251.
- (9) Guillodo, M.; Vernoux, P.; Fouletier, J. *Solid State Ionics* **2000**, *127*, 99.
- (10) Lin, Y.; Zhan, Z.; Barnett, S. A. *J. Power Sources* **2006**, *158*, 1313–1316.
- (11) Xiao, G.; Chen, F. *Electrochem. Commun.* **2011**, *13*, 57–59.
- (12) Muñoz-García, A. B.; Bugaris, D. E.; Pavone, M.; Hodges, J. P.; Huq, A.; Chen, F.; zur Loye, H.-C.; Carter, E. A. *J. Am. Chem. Soc.* **2012**, *134*, 6826–6833.
- (13) Muñoz-García, A. B.; Pavone, M.; Ritzmann, A. M.; Carter, E. A. *Phys. Chem. Chem. Phys.* **2013**, *15*, 6250–6259.
- (14) Xiao, G. L.; Liu, Q.; Wang, S. W.; Komvokis, V. G.; Amiridis, M. D.; Heyden, A.; Ma, S. G.; Chen, F. L. *J. Power Sources* **2012**, *202*, 63–69.
- (15) Xiao, G.; Liu, Q.; Nuansaeng, S.; Chen, F. *ECS Trans.* **2012**, *45*, 355–362.
- (16) Liu, Q.; Dong, X.; Xiao, G.; Zhao, F.; Chen, F. *Adv. Mater.* **2010**, *22*, 5478–5482.
- (17) Liu, G. Y.; Rao, G. H.; Feng, X. M.; Yang, H. F.; Ouyang, Z. W.; Liu, W. F.; Liang, J. K. *J. Alloys Compd.* **2003**, *353*, 42–47.
- (18) Bugaris, D. E.; Hodges, J. P.; Huq, A.; Chance, W. M.; Heyden, A.; Chen, F.; Loye, H.-C. z. *J. Mater. Chem. A* **2014**, *2*, 4045–4054.
- (19) Kresse, G.; Furthmüller, J. *Phys. Rev. B* **1996**, *54*, 11169–11186.
- (20) Kresse, G.; Joubert, D. *Phys. Rev. B* **1999**, *59*, 1758–1775.
- (21) Perdew, J. P.; Burke, K.; Ernzerhof, M. *Phys. Rev. Lett.* **1996**, *77*, 3865–3868.
- (22) Blöchl, P. E. *Phys. Rev. B* **1994**, *50*, 17953–17979.
- (23) Muñoz-García, A. B.; Pavone, M.; Carter, E. A. *Chem. Mater.* **2011**, *23*, 4525–4536.
- (24) Monkhorst, H. J.; Pack, J. D. *Phys. Rev. B* **1976**, *13*, 5188–5192.
- (25) Makov, G.; Payne, M. C. *Phys. Rev. B* **1995**, *51*, 4014–4022.
- (26) Henkelman, G.; Uberuaga, B. P.; Jonsson, H. *J. Chem. Phys.* **2000**, *113*, 9901–9904.
- (27) Heyden, A.; Bell, A. T.; Keil, F. J. *J. Chem. Phys.* **2005**, *123*, 224101.
- (28) Henkelman, G.; Jonsson, H. *J. Chem. Phys.* **1999**, *111*, 7010–7022.
- (29) Olsen, R. A.; Kroes, G. J.; Henkelman, G.; Arnaldsson, A.; Jonsson, H. *J. Chem. Phys.* **2004**, *121*, 9776–9792.
- (30) Buzzi-Ferraris, G. Politecnico di Milano, *BzzMath: Numerical Libraries in C++*, 2012; www.chem.polimi.it/~gbuzzi (accessed May 12, 2014).
- (31) Stegelmann, C.; Andreasen, A.; Campbell, C. T. *J. Am. Chem. Soc.* **2009**, *131*, 13563–13563.
- (32) Stegelmann, C.; Andreasen, A.; Campbell, C. T. *J. Am. Chem. Soc.* **2009**, *131*, 8077–8082.
- (33) Ammal, S. C.; Heyden, A. *J. Chem. Phys.* **2010**, *133*, 164703.
- (34) Nørskov, J. K.; Rossmeisl, J.; Logadottir, A.; Lindqvist, L.; Kitchin, J. R.; Bligaard, T.; Jonsson, H. *J. Phys. Chem. B* **2004**, *108*, 17886–17892.

- (35) Atkins, P. W. *Physical Chemistry*, 6th ed.; Oxford University Press: Oxford, 1998.
- (36) Laursen, S.; Linic, S. *J. Phys. Chem. C* **2009**, *113*, 6689–6693.
- (37) Laursen, S.; Linic, S. *Phys. Chem. Chem. Phys.* **2009**, *11*, 11006–11012.
- (38) Rogal, J.; Reuter, K.; Scheffler, M. *Phys. Rev. B* **2007**, *75*, 205433.
- (39) Sun, C. W.; Stimming, U. *J. Power Sources* **2007**, *171*, 247–260.
- (40) Kröger, F. A.; Vink, H. J. *Solid State Phys.* **1956**, *3*, 307–435.
- (41) Xiao, G. L.; Liu, Q. A.; Zhao, F.; Zhang, L.; Xia, C. R.; Chen, F. *L. J. Electrochem. Soc.* **2011**, *158*, B455–B460.
- (42) Sun, C. W.; Hui, R.; Roller, J. *J. Solid State Electrochem.* **2010**, *14*, 1125–1144.
- (43) Nelson, G. J.; Nakajo, A.; Cassenti, B. N.; DeGostin, M. B.; Bagshaw, K. R.; Peracchio, A. A.; Xiao, G. L.; Wang, S.; Chen, F. L.; Chiu, W. K. S. *J. Power Sources* **2014**, *246*, 322–334.
- (44) Ingram, D. B.; Linic, S. *J. Electrochem. Soc.* **2009**, *156*, B1457–B1465.
- (45) Mukherjee, J.; Linic, S. *J. Electrochem. Soc.* **2007**, *154*, B919–B924.
- (46) NIST Chemistry WebBook; <http://webbook.nist.gov/chemistry> (accessed May 12, 2014).
- (47) Bard, A. J.; Faulkner, L. R. *Electrochemical Methods: Fundamentals and Applications*; 2nd ed.; John Wiley & Sons: New York, 2001.
- (48) Ammal, S. C.; Heyden, A. *J. Phys. Chem. C* **2012**, *116*, 1624–1624.
- (49) Ammal, S. C.; Heyden, A. *J. Phys. Chem. C* **2011**, *115*, 19246–19259.
- (50) Aranifard, S.; Ammal, S. C.; Heyden, A. *J. Phys. Chem. C* **2012**, *116*, 9029–9042.
- (51) Ammal, S. C.; Heyden, A. *J. Phys. Chem. Lett.* **2012**, *3*, 2767–2772.
- (52) Bader, R. F. W. *Atoms in Molecules – A Quantum Theory*; Oxford University Press: New York, 1990.
- (53) Tang, W.; Sanville, E.; Henkelman, G. *J. Phys.: Condens. Matter* **2009**, *21*, 084204.
- (54) Shishkin, M.; Ziegler, T. *J. Phys. Chem. C* **2010**, *114*, 21411–21416.